

Received January 29, 2020, accepted February 28, 2020, date of publication March 5, 2020, date of current version March 17, 2020.

Digital Object Identifier 10.1109/ACCESS.2020.2978638

Roughness Analysis of Sea Surface From Visible Images by Texture

HAILANG PAN^{1,2}, PEILIN GAO¹, HUICHENG ZHOU¹, RUIXUE MA¹, JINGSONG YANG^{2,3}, AND XIN ZHANG⁴

¹School of Electronic and Optical Engineering, Nanjing University of Science and Technology, Nanjing 210094, China

²State Key Laboratory of Satellite Ocean Environment Dynamics, Second Institute of Oceanography, Ministry of Natural Resources, Hangzhou 310012, China

³Southern Marine Science and Engineering Guangdong Laboratory (Zhuhai), Zhuhai 519082, China

⁴Scripps Institution of Oceanography, University of California at San Diego, La Jolla, CA 92093-0213, USA

Corresponding author: Jingsong Yang (jsyang@sio.org.cn)

This work was supported in part by the National Natural Science Foundation of China under Grant 41676167 and Grant 41621064, and in part by the Open Fund of State Key Laboratory of Satellite Ocean Environment Dynamics of China under Grant SOED1009 and Grant QNHX1606.

ABSTRACT This paper presents a roughness analysis of sea surface from visible images by feature measurements of texture for the first time. The algorithms presented in this paper include six texture feature measurements of sea surface use gray level co-occurrence matrix, gray level-gradient co-occurrence matrix, Tamura texture feature, autocorrelation function, edge frequency and fractional Brownian motion autocorrelation. The empirical relationship between wind speeds (or sea surface roughness) and image texture roughness are estimated based on the extracted data. Our experiments have demonstrated that our texture methods and empirical relation between wind speeds and image texture roughness can potentially be used to analyze sea surface roughness from visible images.

INDEX TERMS Sea surface roughness, gray level co-occurrence matrices, gray level-gradient co-occurrence matrices, tamura texture features, autocorrelation function, edge frequency, fractional Brownian motion.

I. INTRODUCTION

Light reflected and scattered from a sea surface flooded with random surface waves and wave breakers is depended on the surface geometry. For example, wavy surface slope forms alternating reflection intensity variations in the observed surface images. While the wave fields at sea are random, waves and their surface shapes do attend to statistical equilibrium states under steady wind conditions [1]. Geometrical surface roughness is closely related to dynamical surface roughness of surface wind-wave boundary layers. Our hypothesis is that the image of surface wavy pattern can be measured as texture roughness which is related to the sea surface roughness. One motivation of our research is to build up a capacity for ocean wave observations, measurements, 3D reconstructions, and property estimations based on wave features extracted from 2D visible images. These approaches can also be applied to analysis of other reflecting surfaces of transparent or opaque objects.

The associate editor coordinating the review of this manuscript and approving it for publication was Vladimir M. Mladenovic¹.

Sea surface roughness is a critical parameter affecting momentum exchanges between air and sea. Zhang *et al.* [2] evaluated the effect of sea surface roughness on ocean surface wave with a coupled atmosphere-wave-ocean model. Observational studies about the sea surface roughness are used the coupled model calculations. A typical typhoon case Vongfong is chosen to examine the effect of sea surface roughness on typhoon wave modeling. Their results indicate that the distribution of significant wave height is obviously affected by the sea surface roughness.

In the past, a number of analysis methods of sea surface roughness have been proposed for optical, microwave, and radio remote measurements. During the Southern Ocean Waves Experiment (SOWEX) an aircraft carried a downward-looking video camera to document the sea surface. Walsh *et al.* [3] developed a numerical simulation scheme that relates image contrast to the gravity-capillary waves's contribution to the sea-surface mean square slope (MSS). A simple optical model for the small-scale roughness of the water is proposed to relate the appearance of the aircraft image in the video to the small-scale MSS.

Crossingham *et al.* [4] described a laser slope gauge that uses a digital technique to measure the refraction angle of a laser beam after the beam has passed through the air-sea interface. It can be a useful and reliable tool for all types of water surface roughness measurements. Burrage *et al.* [5] described an airborne experiment that an L-band microwave radiometer was used for retrieving sea surface salinity (SSS), and L- and S-band reflectometer systems were used to retrieve sea surface roughness (SSR) descriptors including mean square slope and wind speed under a range of surface wind and wave conditions. Hollinger [6] found a definite frequency-dependent correlation between wind speed and microwave brightness temperature of passive microwave from the sea surface. Freedman *et al.* [7] introduced the aquarius scatterometer, a total-power L-band radar system, for estimating ocean surface roughness. This is a relatively simple low-spatial resolution power-detecting radar, without ranging capability. Garrison *et al.* [8] made use of the global positioning system (GPS) delay mapping receiver from the NASA Langley Research Center to generate post-correlation power-versus-delay measurements from GPS signals reflected from the ocean surface. These data were used to estimate ocean surface roughness. Initial results suggest that reflected GPS measurements with small low-power instruments can be used to correct the roughness effects in radiometer brightness temperature measurements to retrieve SSS more accurately.

Surface roughness affects propagation of electromagnetic waves in the surface boundary layers. Zhao *et al.* [9] carried out a study of the influence of sea surface roughness on the electromagnetic wave propagation in a duct environment. The roughness of the sea surface is computed by modifying the smooth surface Fresnel reflection coefficient to account for the reduction in the specular reflection due to the surface roughness resulting from sea wind. Benhmammouch *et al.* [10] studied effects of sea surface roughness on electromagnetic waves propagation in a three-dimensional domain. The 3D parabolic equation method is used to solve the wave equation. A new approach is proposed to model the propagation above rough sea surface. Bass *et al.* [11] described experiments on scattering of radio waves from a rough sea surface. Amplitude, frequency, and space-time characteristics of scattered radio signals at different states of the sea surface are presented. Inversely, parameters of sea roughness can be determined by characteristics of scattered radio signals. Guissard [12] discussed the description of the ocean surface by a vertical displacement spectrum for microwave remote sensing applications. Berizzi *et al.* [13] showed a method of fractal analysis of ERS-1 SAR images, and presented the results obtained by three different algorithms. Fractal dimension of the sea surface is closely related to its roughness. Garelo *et al.* [14] outlined a method for simulating the ocean surface as seen by a space borne SAR. A statistical approach was chosen in order to integrate the different mechanisms responsible for the imaging of the surface waves. A 2D sea-state surface was simulated, then divided in facets and each facet was given

a statistical behaviour under a surface constraint. Different parameters may be adjusted in the simulations, such as swell direction or sea-state roughness.

Detecting and understanding sea surface roughness are important in a range of oceanographic application. Weissman and Bourassa [15] studied changes in the sea surface roughness from the combined effects of wind and rain, on scales of tens of kilometers using the QuikSCAT scatterometer (NRCS) and simultaneous NEXRAD three-dimensional measurements of rain. Tanck *et al.* [16] presented a new method for extracting the rms height and correlation length of sand ripples on tidal flats from multi-frequency synthetic aperture radar (SAR) data. The normalized radar cross section (NRCS) of tidal flats that are covered with sand ripples is a function of the soil moisture as well as of the surface roughness. The variation of the NRCS is dominated by variations of the surface roughness. Stolte [17] published radar, sonar and roughness experiments. The roughness conditions can be characterized by three wind speed ranges: wind below 2.5 m/s, increasing wind up to 15 m/s, and higher wind speed. Radar backscatter and sonar conditions reflect these characteristics. Hamlington *et al.* [18] positively identified the 2010 Chilean tsunami in satellite altimeter measurements of sea surface roughness. It is likely that tsunami-induced changes in sea surface roughness are observable with other types of space- and airborne sensors. Pan *et al.* [19] presented fractal dimension measurements of sea surface from nearshore single images by six fractal methods.

Our research focuses mainly on three aspects: texture measurements from visible images, estimations of wind speed (or sea surface roughness) functional dependency on texture features based on the extracted data, and sensitivity of the methods through tests under four type noises. This paper is organized as follows: Section 2 presents the texture measurements of sea surface from visible images by gray level co-occurrence matrix (GLCM), gray level-gradient co-occurrence matrix (GLGCM), Tamura texture feature (TTF), autocorrelation function (ACF), edge frequency (EF) and fractional Brownian motion autocorrelation (FBMA) approaches. Section 3 presents relations between sea surface roughness and wind speed. Section 4 presents the experimental results of texture measurements, empirical fittings, error analysis, effects of four noises and so on.

II. TEXTURE MEASUREMENTS

In analysis surface wave dynamics, it is convenient to describe the shape of sea surface in Fourier linear expansion. However, an ocean wave field is a nonlinear and random process. For the purpose of extracting wave field statistical parameters, such as surface roughness, it is more efficient, we believe, to represent the surface image directly by nonlinear descriptors, such as texture features attempted in this paper. This section describes how to perform texture measurements of sea surface from nearshore still images by six texture methods, which are gray level co-occurrence matrix, gray level-gradient co-occurrence matrix, autocorrelation

function, FBM autocorrelation, edge frequency and Tamura texture feature methods.

A. GRAY LEVEL CO-OCCURRENCE MATRICES

This section describes the texture measurements of sea surface from nearshore still optical images by the approach of gray level co-occurrence matrix (GLCM).

1) DEFINITION

Let us suppose that the analyzed image is rectangular and has N_x columns and N_y rows, and the gray level appearing at each pixel is digitized into N_g levels. Let $X = \{1, 2, 3, \dots, N_x\}$, $Y = \{1, 2, 3, \dots, N_y\}$, and $G = \{0, 1, 2, \dots, N_g - 1\}$ be the sets of column index, row index, and gray level values respectively. The set $X \times Y$ is the coordinate set of image pixels ordered by their row-column designations. Thus, our images can be represented as a function that assigns some gray level in G to each pixel or pair of coordinates in $X \times Y$; $f: X \times Y \rightarrow G$.

One way of specifying the image texture-context feature is through the matrix of relative frequencies. It is constructed as following: for any two separated pixels with gray level i and j separated by distance d in the direction θ in an interest region of an image, we calculate the frequency of appearance of the pixel combination in the image noted as $P(i, j, d, \theta)$.

$$P(i, j, d, \theta) = \# \{[(k, l)(m, n)] \in (L_y \times L_x) \times (L_y \times L_x) \mid f(k, l) = i, f(m, n) = j, d, \theta\} \quad (1)$$

where $\#$ denotes the number of elements in the set.

For a specific case that angle, θ , is quantized into 45° intervals, the four unnormalized frequencies are defined by:

$$\begin{aligned} P(i, j, d, 0^\circ) &= \# \{[(k, l)(m, n)] \in (L_y \times L_x) \times (L_y \times L_x) \mid k - m = 0, |l - n| \\ &= d, I(k, l) = i, I(m, n) = j\} \end{aligned} \quad (2)$$

$$\begin{aligned} P(i, j, d, 45^\circ) &= \# \{[(k, l)(m, n)] \in (L_y \times L_x) \times (L_y \times L_x) \mid (k - m = d, l - n = -d) \text{ or } (k \\ &- m = -d, l - n = d), I(k, l) = i, I(m, n) = j\} \end{aligned} \quad (3)$$

$$\begin{aligned} P(i, j, d, 90^\circ) &= \# \{[(k, l)(m, n)] \in (L_y \times L_x) \times (L_y \times L_x) \mid |k - m| = d, l - n \\ &= 0, I(k, l) = i, I(m, n) = j\} \end{aligned} \quad (4)$$

$$\begin{aligned} P(i, j, d, 135^\circ) &= \# \{[(k, l)(m, n)] \in (L_y \times L_x) \times (L_y \times L_x) \mid (k - m = d, l - n = d) \text{ or } (k - m \\ &= -d, l - n = -d), I(k, l) = i, I(m, n) = j\} \end{aligned} \quad (5)$$

The distance d and direction θ are to be specified with the proper value according to a particular application, and are used to compose all the available $P(i, j, d, \theta)$ in the research region.

2) TEXTURAL FEATURES

In order to estimate the similarity between different gray level co-occurrence matrices, Haralick *et al.* [20] proposed 14 statistical features extracted from them. To reduce the computational complexity, only energy (ASM), correlation (COR), contrast (CON), entropy (ENT) and inverse difference moment (IDM) are applied to represent the surface roughness features.

1) Angular second moment (or Energy):

$$ASM = \sum_{i=0}^{g-1} \sum_{j=0}^{g-1} P^2(i, j, d, \theta) \quad (6)$$

2) Contrast:

$$CON = \sum_{i=0}^{g-1} \sum_{j=0}^{g-1} (i - j)^2 \times P^2(i, j, d, \theta) \quad (7)$$

3) Entropy:

$$ENT = - \sum_{i=0}^{g-1} \sum_{j=0}^{g-1} P(i, j, d, \theta) \log P(i, j, d, \theta) \quad (8)$$

4) Inverse difference moment:

$$IDM = \sum_{i=0}^{g-1} \sum_{j=0}^{g-1} \frac{P(i, j, d, \theta)}{1 + (i - j)^2} \quad (9)$$

5) Correlation:

$$COR = \sum_{i=0}^{g-1} \sum_{j=0}^{g-1} \frac{i \times j \times P(i, j, d, \theta) - \mu_1 \times \mu_2}{\sigma_1^2 \times \sigma_2^2} \quad (10)$$

where

$$\begin{aligned} \mu_1 &= \sum_{i=0}^{g-1} i \sum_{j=0}^{g-1} P(i, j, d, \theta) \\ \mu_2 &= \sum_{j=0}^{g-1} j \sum_{i=0}^{g-1} P(i, j, d, \theta) \\ \sigma_1 &= \sum_{i=0}^{g-1} (i - \mu_1)^2 \sum_{j=0}^{g-1} P(i, j, d, \theta) \\ \sigma_2 &= \sum_{j=0}^{g-1} (j - \mu_2)^2 \sum_{i=0}^{g-1} P(i, j, d, \theta) \end{aligned}$$

3) FEATURE PROPERTIES

GLCM is a symmetric matrix, and its order is decided by the gray-scale order of the image.

Contrast is a measure of the amount of local variations present in an image. For an image with smooth surface profile, with low levels of local variation, the entries in the

GLCM will be clustered along the diagonal of the array, consequently producing a low value of contrast. On the other hand, a high value of contrast implies that the image has a rough surface profile.

Autocorrelation is a measure of grey level linear dependencies in the image. A high value of autocorrelation implies a linear relationship between the grey levels of cell pairs, and hence, a smooth surface profile.

Energy provides a measure of repeated transitions of the cell pairs, which indicates textural uniformity. High values of energy occur when the grey level distribution in the image has either a constant or periodic form, with the vector displacements often falling on the same (i, j) grey level pair.

Entropy is a measure of randomness of the image. If the image is not texturally uniform, many elements in the GLCM will have low values and hence, the entropy will be large.

4) DISPLACEMENT PARAMETER DETERMINATION

The displacement parameter d is important in the computation of GLCM. Applying a large displacement parameter value to a fine texture would yield a co-occurrence matrix that does not capture the textural information, and vice versa. A displacement parameter value equal to the size of the texture element would tend to improve the classification result with texture features.

For displacement parameter determination of our experiment, we use $d = 1, 2, \dots, 10$ and 10 as our upper limit of range. Fig.1 shows the graphs of texture values (ASM , CON , ENT and IDM) versus quantization schemes. Four orientations of 0° (blue solid), 45° (cyan solid), 90° (green solid) and 135° (black solid) are selected for parameter determination.

Several conclusions have been drawn from this experiment, as follows:

(1) ASM and IDM decrease with the increase of d . ASM remain stable in the range of $d = 5 \sim 10$ and IDM is stable between $d = 6$ and 10.

(2) ENT and CON increase with the increase of d . ENT remain stable from $d = 4$ to 10 and CON become stable starting from $d = 5$.

(3) The orientation parameter θ is relatively less important compared to other factors in co-occurrence matrices, so we use $\theta = 0^\circ, 45^\circ, 90^\circ$ and 135° for they cover efficiently all directions of sea surface images.

5) INTEGRATED FREQUENCIES

In order to take into account the information in four orientations and their proportions, we use integrated frequencies to represent texture features of sea surface, as follows:

$$P(i, j) = aP(i, j, d, 0^\circ) + bP(i, j, d, 45^\circ) + cP(i, j, d, 90^\circ) + eP(i, j, d, 135^\circ) \quad (11)$$

where

$$a + b + c + e = 1$$

$$a = \frac{m_0}{(m_0 + m_{45} + m_{90} + m_{135})}$$

TABLE 1. The calculated weights of integrated frequency.

	$a (\theta=0^\circ)$	$b (\theta=45^\circ)$	$c (\theta=90^\circ)$	$e (\theta=135^\circ)$
ASM	0.21	0.26	0.26	0.27
CON	0.14	0.28	0.25	0.33
ENT	0.15	0.29	0.27	0.29
IDM	0.22	0.26	0.26	0.26

$$b = \frac{m_{45}}{(m_0 + m_{45} + m_{90} + m_{135})}$$

$$c = \frac{m_{90}}{(m_0 + m_{45} + m_{90} + m_{135})}$$

$$e = \frac{m_{135}}{(m_0 + m_{45} + m_{90} + m_{135})}$$

$$m_i = \frac{1}{f_i - f_{ave} + 1} \quad (12)$$

where f is ASM , CON , ENT or IDM .

The calculated weights a , b , c , e of integrated frequency $P(i, j)$ are listed in TABLE 1.

B. GRAY LEVEL-GRADIENT CO-OCCURRENCE MATRICES

The gray level co-occurrence matrix method, for an example 2-D histogram, is frequently used in various applications. However, the gray level-gradient co-occurrence matrix (GLGCM) takes into account the information of both gray level and gradient among pixels in an image [21]. The element $h(i, j)$ of GLGCM is defined as the probability of the pixel number which has gray value i in the normalized gray-level image $F(m, n)$ and gradient value j in the normalized gradient image $G(m, n)$. Therefore, the gray level-gradient co-occurrence matrix provides the space relationship pixels and their adjacent pixels.

In order to avoid complicated calculations, first, we normalize gray-level image and gradient image. The gradient level normalization has the equation form of

$$G(m, n) = INT\left[\frac{g(m, n) \times N_s}{g_{max}}\right] + 1 \quad (13)$$

where $g(m, n)$ is the gradient image, g_{max} is the maximum gradient value in matrix g . N_s is normalized maximum gradient value. We set $N_s = 128$.

The gray level normalization has the equation form of

$$F(m, n) = INT\left[\frac{f(m, n) \times N_g}{f_{max}}\right] + 1 \quad (14)$$

where $f(m, n)$ is the gray-level image, f_{max} is the maximum gray value of matrix f . N_g is the maximum gray value after normalization. We set $N_g = 128$.

Then, H_{ij} is found from counting the number of pixels which satisfy $F(m, n) = i$ and $G(m, n) = j$. The total amount of H_{ij} are calculated by the equation (15)

$$H = \sum_{i=1}^{N_g} \sum_{j=1}^{N_s} H_{ij} \quad (15)$$

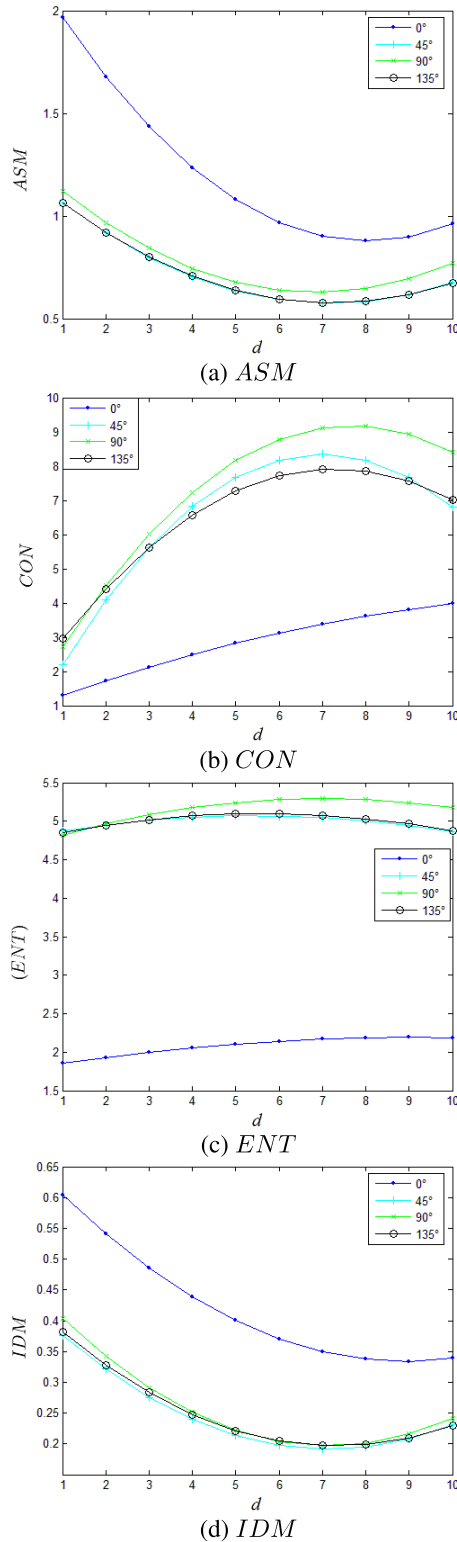


FIGURE 1. Relations of textural features and displacement parameter d .

Then the normalized GLGCM P_{ij} can be found as

$$P_{ij} = \frac{H_{ij}}{N_g \times N_s} \quad (16)$$

where $i = 1, 2, \dots, N_g, j = 1, 2, \dots, N_s$.

Fifteen texture features can be extracted from the GLGCM, such as small-grads advantage, large-grads advantage, gray level asymmetry, and so on. We select *Energy* to represent sea surface roughness. It reflects the uniformity of the gray level distribution of image. *Energy* is large for coarse textures, and small for fine textures.

$$Energy = \sum_{i=1}^{N_g} \sum_{j=1}^{N_s} P_{ij}^2 \quad (17)$$

The origin of GLGCM is in the upper left corner of image. The gray axis is vertical downward through the origin, that is, gray level increase with the increase of i . The gradient axis is horizontal to the right, that is, gradient level increase with the increase of j . For coarse texture images, $H(i, j)$ are mainly distributed near the gray axis and only a few are away from it. For fine texture images, $H(i, j)$ are all scattered along the gradient axis.

C. TAMURA TEXTURE FEATURES

The coarseness gives information about the size of the texture elements. The higher the coarseness value is, the rougher is the texture. If there are two different textures, one macro texture of high coarseness and one micro texture of low coarseness, then, the macro texture is only considered. The essence of calculating the coarseness value is to use operators of various sizes. A large size operator is chosen when a coarse texture is present even if there is a micro-texture and a small operator is chosen when micro texture is present only [21]. The coarseness measure is calculated as follows:

Step1: Taking the average at every pixel over neighborhoods whose sizes are the power of two. The average over the neighborhood of size $2^k \times 2^k$ ($k = 0, 1, 2, 3, 4, 5$) at every pixel is:

$$A_k(x, y) = \frac{1}{2^{2k}} \sum_{i=x-2^{k-1}}^{x+2^{k-1}-1} \sum_{j=y-2^{k-1}}^{y+2^{k-1}-1} g(i, j) \quad (18)$$

where $g(i, j)$ is the gray-level at (i, j) .

Step2: For each pixel, calculating the differences between the non-overlapping neighborhoods on horizontal and vertical directions:

$$E_{k,h}(x, y) = |A_k(x + 2^{k-1}, y) - A_k(x - 2^{k-1}, y)| \quad (19)$$

$$E_{k,v}(x, y) = |A_k(x, y + 2^{k-1}) - A_k(x, y - 2^{k-1})| \quad (20)$$

Step3: For each pixel, selecting the best size which gives the highest output value:

$$S_{best}(x, y) = 2^k + 1 \quad (21)$$

where k maximizes E in either direction:

$$E_k(x, y) = \max(E_{k,h}(x, y), E_{k,v}(x, y)) \quad (22)$$

Step4: Taking the average of S_{best} over the image to be the coarseness measure F_{crs} :

$$F_{crs} = \frac{1}{m \times n} \sum_{i=1}^m \sum_{j=1}^n S_{best}(i, j) \quad (23)$$

where m and n are the effective width and height of the image respectively.

Apparently, F_{crs} describes the texture roughness characteristic of sea surface images. The method of Tamura texture feature is more intuitive to human visual perception than other roughness extraction methods.

D. AUTOCORRELATION FUNCTION

Autocorrelation function can be used to describe the image texture roughness and periodicity according to the correlation between a particular pixel and its neighborhood pixels. Image texture roughness can be represented by the decline speed of its autocorrelation function [21].

Autocorrelation function is defined as

$$C(\varepsilon, \eta) = \frac{\sum_{i=1}^{N_x} \sum_{j=1}^{N_y} f(i, j) f(i + \varepsilon, j + \eta)}{\sum_{i=1}^{N_x} \sum_{j=1}^{N_y} f(i, j)^2} \quad (24)$$

where $f(x, y)$ is original image, $x = 1, 2, \dots, N_x$, $y = 1, 2, \dots, N_y$.

Autocorrelation function, the correlation of all image pixels and their adjacent pixels with a certain distance, can be used to describe image texture feature. Image roughness, regularity and other visual features of image texture can be obtained by evaluating the relationship between autocorrelation function $C(\varepsilon, \eta)$ and parameters ε, η , for example, by the decline speed of autocorrelation function with the increase of ε, η . If autocorrelation function declines slowly with the increase of ε, η , then the texture is smooth, and vice versa. In order to accurately reflect the correlation between specified pixel and its neighborhood pixel, we set ε, η between 1 and 10.

For given ε, η values, correlation between pixels in the coarse texture region is higher than that in the fine texture region. In order to quantitatively calculate the image roughness, we select the second order moment as a measure, which is defined as:

$$T(\varepsilon, \eta) = \sum_{\varepsilon} \sum_{\eta} \varepsilon^2 \eta^2 C(\varepsilon, \eta) \quad (25)$$

$T(\varepsilon, \eta)$ value is higher, image texture will be more rough.

E. EDGE FREQUENCY

The texture image to be analyzed is a two-dimensional function $\{f(x, y), x = 1, 2, \dots, M, y = 1, 2, \dots, N\}$, the gray value of each pixel is regarded as the function value. Edge point detection is to calculate local maximum value and its corresponding direction of the gradient of $f(x, y)$ [21].

The gradient of $f(x, y)$ in the direction θ and along r is defined as:

$$\frac{\partial f}{\partial r} = \frac{\partial f}{\partial x} \frac{\partial x}{\partial r} + \frac{\partial f}{\partial y} \frac{\partial y}{\partial r} = f_x \cos \theta + f_y \sin \theta \quad (26)$$

where the maximum value of $\frac{\partial f}{\partial r}$ can be found by letting $\frac{\partial(\frac{\partial f}{\partial r})}{\partial \theta} = 0$.

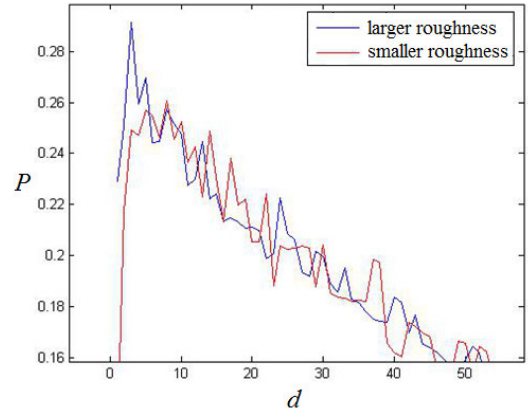


FIGURE 2. Probability distribution comparison of edge point densities of the large and small roughness texture.

The maximum gradient g is used for edge detection.

$$g = \left(\frac{\partial f}{\partial r} \right)_{\max} = \sqrt{f_x^2 + f_y^2} \quad (27)$$

Gradient function $g(d)$ based on the variable distance d between pixels is defined by

$$g(d) = |f(x, y) - f(x + d, y)| + |f(x, y) - f(x - d, y)| \\ + |f(x, y) - f(x, y + d)| + |f(x, y) - f(x, y - d)| \quad (28)$$

where d determines calculated edge size of the gradient function. If the selected d value is small, then $g(d)$ is short edge gradient, else if the selected d value is large, then $g(d)$ is long edge gradient.

After the calculation of the gradient values, the edge point numbers with different d values are calculated. After normalization, probability distribution map of the edge densities P with the change of d values are obtained. When P value is large in the range of small d value, the image texture is fine and there are many short edges in it. When P value is large in the range of large d value, the image texture is coarse and there are many long edges in it.

We choose 1 as the minimum value and $\max(M, N)$ as the maximum value. When d is large enough, P will be 0. For our experiment, we only need to find approximate change trend of d and P and obtain the maximum value P_{\max} .

The texture can be distinguished by the number of edge points in unit area. For small roughness texture, there are relatively small changes in pixels, and the edge point number will be small in unit area. For large roughness texture, there are relatively large changes in pixels, and the edge point number will be large in unit area. In conclusion, the edge density is relatively large for rough texture.

Probability distribution comparison of edge point densities of the large and small roughness texture are shown in Fig.2. The larger the P_{\max} , the greater the roughness, the smaller the P_{\max} , the smaller the roughness. So the maximum value of edge point density is selected to measure roughness.

F. FBM AUTOCORRELATION

Brightness difference of image $I(x, y)$ with step s can be calculated as follows [21]:

$$I(x, y) = f(x, y) - \frac{1}{\#N(s)} \sum_{k, l \in N(s)} f(x + k, y + l) \quad (29)$$

where $f(x, y)$ is original image, $x = 1, 2, \dots, N_x$, $y = 1, 2, \dots, N_y$. $\#N(s)$ is the number of pixels in a ring with inside radius $s-1$ and outer radius s . $N(s)$ can be represented as follows:

$$N(s) = \{k, l \mid (s-1)^2 < k^2 + l^2 \leq s^2\} \quad (30)$$

The autocorrelative function of brightness difference of image $I(x, y)$ can be calculated as follows:

$$R_I(s) = \frac{1}{N_x \times N_y} \sum_{x=1}^{N_x} \sum_{y=1}^{N_y} \left[\frac{I(x, y)}{\#N(s)} \sum_{k, l \in N(s)} I(x + k, y + l) \right] \quad (31)$$

Given two arbitrary natural numbers (s, t) , R can be calculated as follows:

$$R = \ln \left[\frac{R_I(s)}{R_I(t)} \right] / \ln \left[\frac{s}{t} \right] \quad (32)$$

where $0 < R < 1$, $R_I(s)$ is one autocorrelation function with the variable s and $R_I(t)$ is another autocorrelation function with the variable t .

R varies with s and t , and can be used to describe the texture feature of any image. For images with large roughness texture, there is strong correlation between pixels. The calculated autocorrelation functions of brightness difference image with different natural numbers (s, t) have relatively big differences, and calculated R values are all scattered. For images with small roughness texture, the correlation between pixels is weak and the calculated autocorrelation functions will be clustered. The calculated R values are clustered and their distribution is relatively concentrated. According to the change characteristics of R , we can represent the image roughness by calculating its variance D . If the calculated R values are dispersed, the variance and roughness of the image will be larger, else if the calculated R values are concentrated, the variance and roughness of the image will be small, so R can be used to represent the image roughness.

III. EMPIRICAL DEPENDENCE OF SURFACE ROUGHNESS AND IMAGE ROUGHNESS

This section describes our experimental study of measuring surface roughness from images.

A. RELATIONAL EXPRESSION

An empirical relation of sea surface roughness and wind speed at 10 meter height used here is from [22]:

$$z_0 = 0.15(u_{10} - 1.6)^2 + 0.366 \quad (33)$$

where the unit of z_0 is 10^{-4} m.

In our experiments, the actual vertical height between our anemometer and sea surface is 5.28m. Conversion the 10m wind from 5.28m wind is by [23]:

$$u_{10} = 1.08u_{5.28} \quad (34)$$

For this experiment, the actual expression of roughness in term of wind speed becomes:

$$z_0 = 0.15(1.08u_{5.28} - 1.6)^2 + 0.366 \quad (35)$$

B. ERROR ANALYSIS

Mean square error (MSE) and relative error (RE) are utilized as evaluation criterion. Here the MSE is adopted as main criterion because MSE can characterize the prediction accuracy. MSE and RE are defined by

$$MSE = \frac{1}{N} \sum_{i=1}^N (Y_{true} - Y_{pred})^2 \quad (36)$$

$$RE = \frac{1}{N} \sum_{i=1}^N \frac{|Y_{true} - Y_{pred}|}{Y_{true}} \quad (37)$$

where Y_{true} is the measured value, Y_{pred} is the predicted value, and N is the number of prediction samples.

IV. EXPERIMENT RESULTS

This section describes the experimental results on the relationship between wind speeds (or surface roughness) and image texture roughness, error analysis of the six texture methods, effects of four noises (Gaussian, impulse, random and multiplicative noises) and so on.

A. ROUGHNESS ANALYSIS

The data are acquired at a site in Lian island coast of Lianyungang city (China). The site is chosen for the advantages of high wind speed and wave fluctuation, less impurity in seawater and good observation location. A total of 3647 sets of data were collected in this experiment. Each set of data includes one image of sea surface and its corresponding 5.28m wind speed. Image data are collected using single camera with image of 3264 by 2468 pixels (See Fig.3(b)) and wind speed data are obtained by a SMART SENSOR anemometer (AR-816) with an accuracy of 0.1m/s (See Fig.3(a)). The measured values of wind speed are between 0~3.9m/s (weak wind). The horizontal length of the field of view is approximately 6 meters and the vertical width is about 5 meters. The aperture of the camera's lens is F1.8 at 2.0× optical magnification.

In the experiments of roughness analysis of sea surface by the six texture methods (See Fig.4), the values of image texture roughness are extracted from sea surface images first. Then relations between wind speeds (or sea surface roughness) and image texture roughness are constructed by using Whisker charts based on the extracted data. The maximum value of the upper whisker line is the point at which there are 25% data points whose values lie above the maximum value.

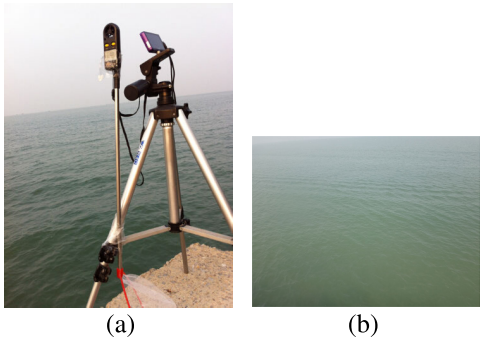


FIGURE 3. (a) View of the vision equipment used for the experiment (b) Original captured image.

TABLE 2. The fitting errors of six texture methods.

	GLCM	GLGCM	TTF	ACF	EF	FBMA
RE	0.1200	0.0926	0.1316	0.0691	0.1442	0.0770
MSE	0.0067	0.0045	0.0074	0.0034	0.0083	0.0036

The minimum value of the lower whisker line is the point at which there are 75% data points whose values lie above the minimum value. The red solid point is the average value of each set of data.

Fig.4 shows that the wind speed gradually increases with the extracted values of image texture roughness. TABLE 2 shows that the fitting accuracies of ACF and FBMA methods are higher than the other four.

B. EFFECTS OF NOISES

Four different types of noises with different parameters are added to the sea surface image to evaluate the noise suppression performances of six texture methods.

1. Gaussian noises

Different Gauss noises are added to the sea surface image for algorithm comparisons. The noise mean values are all set to 0 and variance δ values are 0, 0.02, 0.04, 0.06, 0.08, 0.10, 0.12, 0.14, 0.16 and 0.18 respectively. Examples of images with different δ values of Gauss noises are shown in Fig.5(a). The roughness values obtained by six texture methods can be found in TABLE 3(a).

2. Impulse noises

Different impulse noises are added to the sea surface image for the comparisons. The noise density D values are 0, 0.02, 0.04, 0.06, 0.08, 0.10, 0.12, 0.14, 0.16 and 0.18 respectively. Examples of images with different D values of impulse noises are shown in Fig.5(b) and the roughness values obtained by six texture methods are listed in TABLE 3(b).

3. Random noises

For random noises, the added noise density D values are also 0, 0.02, 0.04, 0.06, 0.08, 0.10, 0.12, 0.14, 0.16 and 0.18 respectively. Examples of images with different D values of random noises are shown in Fig.5(c) and TABLE 3(c) shows the roughness values obtained by six texture methods.

4. Multiplicative noises

Different multiplicative noises are also added to the sea surface image for comparisons. The mean values of noise are all set to 0 and variance values are 0, 0.02, 0.04, 0.06,

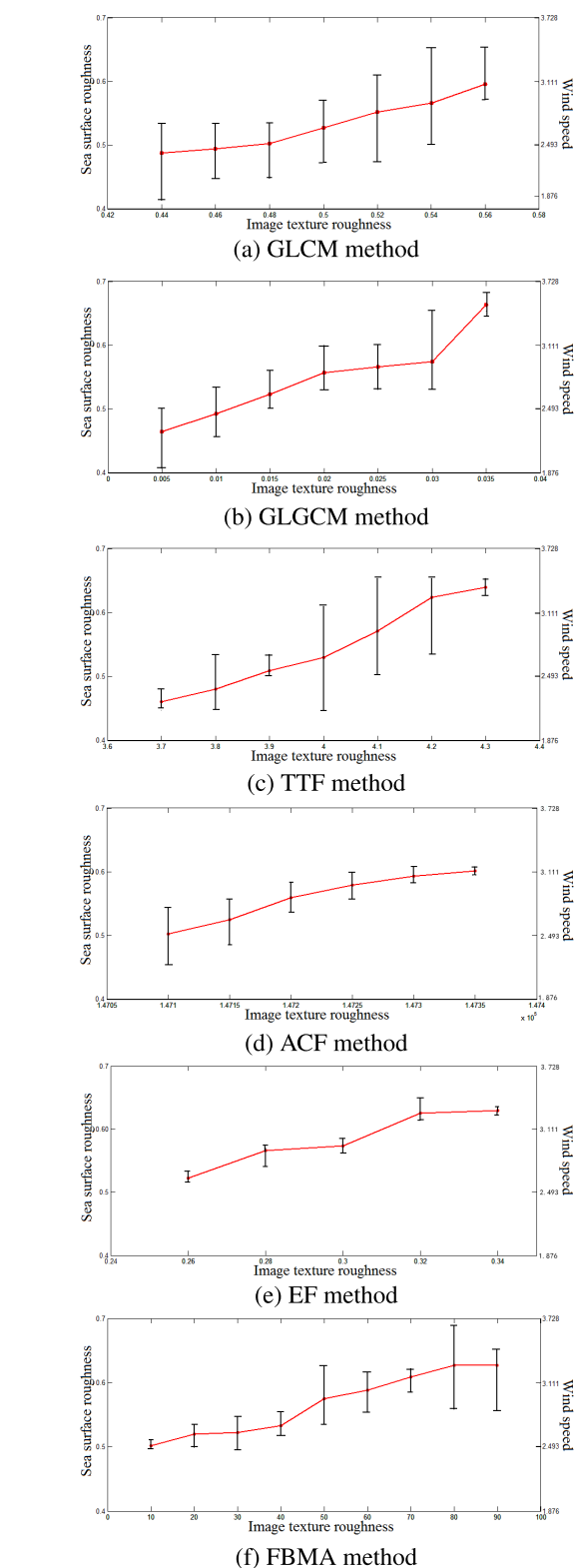


FIGURE 4. The relation schemas of six texture methods.

0.08, 0.10, 0.12, 0.14, 0.16 and 0.18 respectively. Examples of images with different variance values of multiplicative noises are shown in Fig.5(d), and the roughness values obtained by six texture methods are listed in TABLE 3(d).

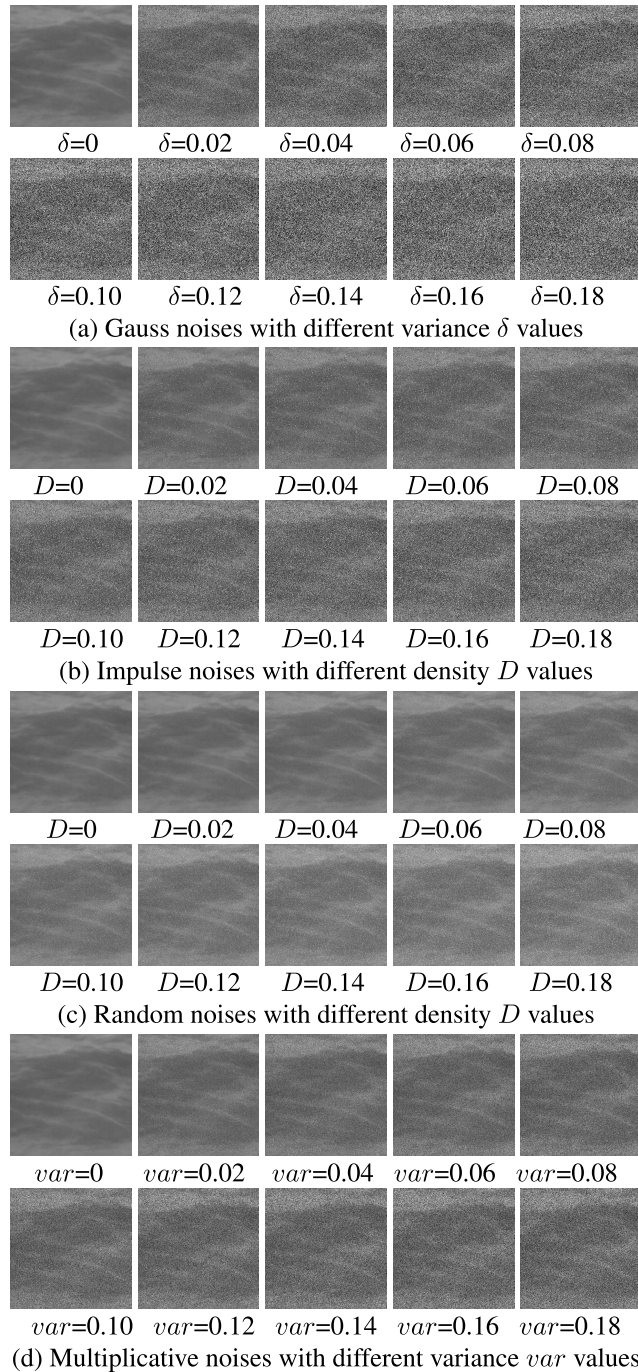


FIGURE 5. Images affected by four noises with different values.

Experimental results show that the roughness values changes with the change of noise parameters. The changes of roughness values in TABLE 3 and Fig. 6 show that the edge frequency method is less affected by noises and has good noise suppression ability.

C. OIL SPILL DETECTION

Oil is one of the major pollutants of the marine environment. It may be introduced in diverse ways, such as natural sources, offshore production, sea traffic, tanker accidents, atmospheric deposition, river run off and dumping. Oil spills

TABLE 3. The roughness values affected by four noises.

(a) Gauss noise						
δ	GLCM	GLGCM	TTF	ACF	EF	FBMA
0	5.02	6.74	4.07	1.41	2.38	1.7244
0.02	3.16	4.20	2.77	0.92	3.38	2.03
0.04	3.16	1.70	2.77	1.28	3.38	1.56
0.06	3.02	1.20	2.76	1.18	3.38	1.87
0.08	3.18	1.10	2.76	1.10	3.38	1.87
0.10	3.20	1.30	2.76	1.05	3.38	1.97
0.12	3.34	1.60	2.76	1.01	3.38	2.43
0.14	3.55	2.10	2.75	0.98	3.38	1.96
0.16	3.60	2.70	2.76	0.96	3.38	1.82
0.18	3.77	3.30	2.75	0.94	3.38	1.75
(b) Impulse noise						
D	GLCM	GLGCM	TTF	ACF	EF	FBMA
0	5.02	6.74	4.07	1.41	2.38	1.7244
0.02	1.23	0.65	3.64	1.15	2.38	2.31
0.04	1.31	1.21	3.36	1.38	2.38	1.44
0.06	1.11	1.37	3.16	1.35	2.38	1.43
0.08	1.34	1.22	3.03	1.31	2.38	1.93
0.10	1.41	1.09	2.94	1.28	2.38	2.17
0.12	1.56	0.97	2.88	1.25	2.38	1.83
0.14	1.51	0.86	2.83	1.23	2.38	1.79
0.16	1.24	0.79	2.81	1.20	2.38	1.86
0.18	1.21	0.71	2.79	1.18	2.38	2.34
(c) Random noise						
D	GLCM	GLGCM	TTF	ACF	EF	FBMA
0	5.02	6.74	4.07	1.41	2.38	1.7244
0.02	1.11	0.55	3.51	1.36	2.38	1.71
0.04	1.21	1.07	3.11	1.42	2.38	1.06
0.06	1.44	0.65	2.94	1.41	2.38	2.83
0.08	1.23	0.60	2.86	1.41	2.38	2.17
0.10	1.51	0.61	2.82	1.40	2.38	1.78
0.12	1.68	0.63	2.80	1.40	2.38	1.52
0.14	1.22	0.60	2.79	1.39	2.38	1.71
0.16	1.35	0.63	2.78	1.38	2.38	1.66
0.18	0.87	0.57	2.77	1.37	2.38	1.78
(d) Multiplicative noise						
var	GLCM	GLGCM	TTF	ACF	EF	FBMA
0	5.02	6.74	4.07	1.41	2.38	1.7244
0.02	0.97	1.10	2.86	1.20	3.32	2.03
0.04	1.98	2.30	2.81	1.39	3.32	1.77
0.06	1.23	1.90	2.79	1.36	3.32	1.72
0.08	1.11	1.70	2.79	1.34	3.32	1.66
0.10	1.32	1.50	2.78	1.31	3.32	1.59
0.12	1.22	1.30	2.78	1.29	3.32	1.94
0.14	1.21	1.20	2.77	1.27	3.32	2.09
0.16	1.35	1.20	2.78	1.24	3.32	1.87
0.18	1.50	1.10	2.77	1.22	3.32	1.84

can seriously affect the marine ecosystem and cause social and scientific concerns since they seriously effect fragile marine and coastal ecosystem. The amount of pollutant discharges and associated effects on the marine environment are important parameters in evaluating sea water quality. Oil spills can easily be seen but it is difficult, even for an expert, to specify the scope of oil spill at sea.

The six texture methods are examined in order to evaluate their performance in surface oil film detection. Fig.7 contains two aerial images with several oil patches. Six regions in Fig.7(a) and seven in Fig.7(b) are selected for analysis. In Fig.7(a), Part 4 and 5 are areas with oil and Parts 1, 2, 3 and 6 are areas without oil. In Fig.7(b), Part 4, 5 and 6 are

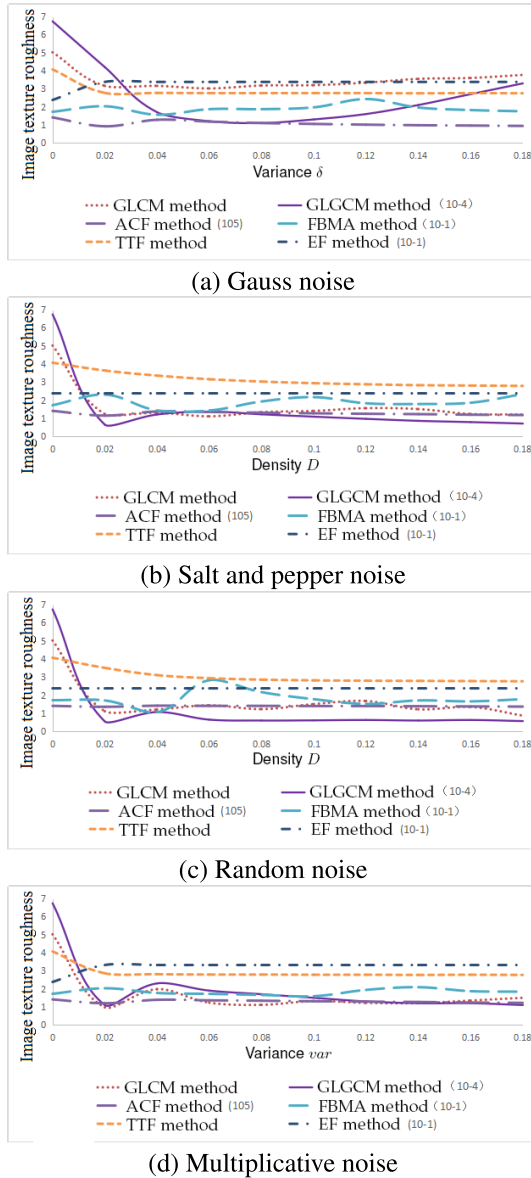


FIGURE 6. The calculated curves of image texture roughness affected by four noises.

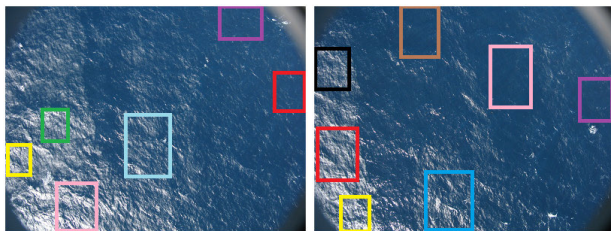


FIGURE 7. Two aerial images with several oil spills.

areas with oil and Parts 1, 2, 3 and 7 are areas without oil. TABLE 4 shows that the GLGCM, EF and GLCM methods have the most discriminating ability because their roughness values of oil contaminated parts are quite different from that without oil. The discriminating abilities of the ACF and TTF methods are the worst because their roughness values are not

TABLE 4. The roughness values of oil parts and no-oil parts.

(a) Image 1						
	GLGCM	EF	GLCM	ACF	FBMA	TTF
Part 1 (pink, no-oil)	0.0003	0.323140	0.01377	101000.623713	0.3757	2.00352
Part 2 (yellow, no-oil)	0.0003	0.303500	0.01443	88002.3765020	0.7412	1.80556
Part 3 (green, no-oil)	0.0004	0.317800	0.01603	82565.1277020	0.2728	1.74260
Part 4 (violet, oil)	0.0015	0.067896	0.62113	109708.880548	0.8874	1.90613
Part 5 (red, oil)	0.0026	0.078645	0.68179	108413.227489	0.7488	1.90360
Part 6 (skyblue, no-oil)	0.0003	0.246930	0.06005	103664.443282	0.1273	2.08916
(b) Image 2						
	GLGCM	EF	GLCM	ACF	FBMA	TTF
Part 1 (black, no-oil)	0.0003	0.254317	0.03168	101480.532853	0.1191	2.01074
Part 2 (red, no-oil)	0.0002	0.315784	0.01364	98721.613427	0.2132	2.13549
Part 3 (yellow, no-oil)	0.0002	0.334906	0.00987	100876.795619	1.0585	2.02367
Part 4 (peru, oil)	0.334906	0.007472	0.34054	108773.354442	0.7098	1.91114
Part 5 (pink, oil)	0.0026	0.048942	0.31530	111209.692669	0.6365	1.93581
Part 6 (violet, oil)	0.0025	0.048942	0.38148	104148.284701	0.6410	1.88359
Part 7 (turquoise, no-oil)	0.0003	0.276845	0.03091	101000.623713	0.0788	2.13366

very different. From the above it can be concluded that the GLGCM, EF and GLCM methods have better performance in oil spill detection than others.

V. CONCLUSION

We have established a new sea surface image analysis technique for extracting sea surface roughness measurements from visible images based on a novel concept of sea surface random field can be represented by texture features. The algorithms presented in this paper include gray level co-occurrence matrix, gray level-gradient co-occurrence matrix, Tamura texture feature, autocorrelation function, edge frequency and fractional Brownian motion autocorrelation approaches. All six texture feature measurements constructed from sea surface images are effective. Our experiments have demonstrated that they all have one-to-one correspondence with sea surface roughness as shown by the empirical relations between wind speeds (or sea surface roughness) and image texture roughness we have found. Our texture methods can analyze sea surface roughness from visible images properly. The autocorrelation function and fractional Brownian motion autocorrelation methods are better in performed error analysis. The edge frequency method performs well under perturbation test by adding four different type noises. The gray level-gradient co-occurrence matrix, edge frequency, and gray level cooccurrence matrix methods have a better performance in oil spill detection. In future we will continue work toward reconstruction 3D sea surfaces and transparent objects from 2D images.

REFERENCES

- [1] O. M. Phillips, "Spectral and statistical properties of the equilibrium range in wind-generated gravity waves," *J. Fluid Mech.*, vol. 156, no. 1, pp. 505–531, Jul. 1985.
- [2] J. Zhang, L. Huang, Y. Wen, and J. Deng, "Numerical simulation of typhoon wave using different sea surface roughness parameterizations in the coupled Atmosphere-Wave-Ocean model," in *Proc. 2nd Int. Conf. Comput. Modeling Simulation*, vol. 1, Jan. 2010, pp. 540–543.
- [3] E. J. Walsh, M. L. Banner, J. H. Churnside, J. A. Shaw, D. C. Vandemark, C. W. Wright, J. B. Jensen, and S. Lee, "Visual demonstration of three-scale sea-surface roughness under light wind conditions," *IEEE Trans. Geosci. Remote Sens.*, vol. 43, no. 8, pp. 1751–1762, Aug. 2005.
- [4] G. J. Crossingham, B. J. Willoughby, D. Ramsdell, and I. S. Robinson, "A digital laser slopometer for small scale sea surface roughness measurements," in *Proc. OCEANS Conf.*, vol. 3, Sep./Oct. 1998, pp. 1676–1680.
- [5] D. Burrage, J. Wesson, D. Wang, J. Garrison, N. Quindara, G. Ganoe, and S. Katzberg, "Airborne Observation of ocean surface roughness variations using a combination of microwave radiometer and reflectometer systems," in *Proc. Workshop Reflectometry GNSS Other Signals Opportunity*, Oct. 2012, pp. 1–7.

- [6] J. Hollinger, "Passive microwave measurements of sea surface roughness," *IEEE Trans. Geosci. Electron.*, vol. 9, no. 3, pp. 165–169, Jul. 1971.
- [7] A. Freedman, D. McWatters, and M. Spencer, "The aquarius scatterometer: An active system for measuring surface roughness for sea-surface brightness temperature correction," in *Proc. IEEE Int. Symp. Geosci. Remote Sens.*, Jul. 2006, pp. 1685–1688.
- [8] J. L. Garrison, J. K. Voo, S. H. Yueh, M. S. Grant, A. G. Fore, and J. S. Haase, "Estimation of sea surface roughness effects in microwave radiometric measurements of salinity using reflected global navigation satellite system signals," *IEEE Geosci. Remote Sens. Lett.*, vol. 8, no. 6, pp. 1170–1174, Nov. 2011.
- [9] X. Zhao, S. Huang, and H. Fan, "Influence of sea surface roughness on the electromagnetic wave propagation in the duct environment," in *Proc. 2nd IITA Int. Conf. Geosci. Remote Sens.*, vol. 1, Aug. 2010, pp. 467–470.
- [10] O. Benhmammouch, N. Caouren, and A. Khenchaf, "Modeling of roughness effects on electromagnetic waves propagation above sea surface using 3D parabolic equation," in *Proc. IEEE Int. Geosci. Remote Sens. Symp.*, vol. 2, Jul. 2009, pp. II-817–II-820.
- [11] F. Bass, S. Braude, I. Fuks, A. Kalmykov, A. Megn, I. Ostrovsky, and A. Rosenberg, "Radiophysical investigations of sea roughness (radiooceanography) at the ukrainian academy of sciences," *IEEE Trans. Antennas Propag.*, vol. 25, no. 1, pp. 43–52, Jan. 1977.
- [12] A. Guissard, "Wave spectrum and roughness spectrum for microwave observation of the oceans," in *Proc. IEEE Int. Geosci. Remote Sens. Symp.*, vol. 2, Aug. 1993, pp. 768–769.
- [13] F. Berizzi, P. Gamba, A. Garzelli, G. Bertini, and F. Dell'Acqua, "Fractal behavior of sea SAR ERS-1 images," in *Proc. IEEE Int. Geosci. Remote Sens. Symp.*, vol. 2, Jun. 2002, pp. 1114–1116.
- [14] R. Garelo, S. Proust, and B. Chapron, "2D ocean surface SAR images simulation: A statistical approach," in *Proc. OCEANS*, vol. 3, Oct. 1993, pp. III7–III12.
- [15] D. E. Weissman and M. A. Bourassa, "Measurements of the effect of rain-induced sea surface roughness on the QuikSCAT scatterometer radar cross section and wind stress," in *Proc. OCEANS*, Sep. 2008, pp. 1–4.
- [16] G. Tanck, W. Alpers, and M. Gade, "Determination of surface roughness parameters of tidal flats from SIR-C/X-SAR 3-frequency SAR data," in *Proc. IEEE Int. Geosci. Remote Sens. Symp. (IGARSS)*, vol. 3, Jul. 1999, pp. 1677–1679.
- [17] S. Stolte, "Short scale roughness of the sea, radar backscatter and sonar conditions," in *Proc. Int. Geosci. Remote Sens. Symp.*, vol. 2, May 1992, pp. 862–864.
- [18] B. D. Hamlington, R. R. Leben, O. A. Godin, and V. G. Irisov, "On the feasibility of tsunami detection using satellite-based sea surface roughness measurements," in *Proc. IEEE Int. Geosci. Remote Sens. Symp.*, Jul. 2010, pp. 3035–3038.
- [19] H. L. Pan, W. Jiang, B. Long, P. Wang, J. S. Yang, and X. Zhang, "Roughness change analysis of sea surface from visible images by fractals," *IEEE Access*, to be published.
- [20] R. M. Haralick, K. Shanmugam, and L. Dinstein, "Textural features for image classification," *IEEE Trans. Syst., Man, Cybern.*, vol. SMC-3, no. 6, pp. 610–621, Nov. 1973.
- [21] L. Ma and Y. L. Fan, *Image Texture Analysis*. Beijing, China: Science Press, Sep. 2009.
- [22] K. Xiong, "Observational research on turbulent fluxes, roughness length and drag coefficient over West Pacific tropical ocean area," *Scientia Atmos. Sinica*, vol. 14, no. 4, pp. 475–482, Dec. 1990.
- [23] Y. L. Chen, Y. Zhao, B. Zhang, and L. Yiang, "The study of the relation of wind velocity at different heights over the sea," *Mar. Sci.*, vol. 13, no. 3, pp. 27–31, May 1989.

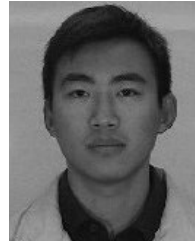


ests include computer vision, computer graphics, and image processing.

HAILANG PAN received the Ph.D. degree in image processing and pattern recognition from Shanghai Jiao Tong University, in 2006. He joined NJUST, in 2007. He is currently an Associate Professor with the School of Electronic and Optical Engineering, Nanjing University of Science and Technology (NJUST). He made many progresses in the research of image analysis and 3D reconstruction of human motion, meteorological maps, and transparent objects. His research interests include computer vision, computer graphics, and image processing.



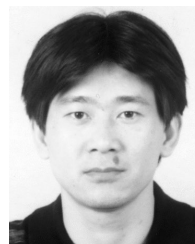
PEILIN GAO received the M.S. degree in information and communication engineering from the School of Electronic and Optical Engineering, Nanjing University of Science and Technology, in 2015.



HUICHENG ZHOU received the M.S. degree in information and communication engineering from the School of Electronic and Optical Engineering, Nanjing University of Science and Technology, in 2018.



RUIXUE MA received the B.S. degree in electronic information engineering from the School of Electronic and Optical Engineering, Nanjing University of Science and Technology, in 2016.



JINGSONG YANG received the B.S. degree in physics and the M.S. degree in theoretical physics from Zhejiang University, Hangzhou, China, in 1990 and 1996, respectively, and the Ph.D. degree in physical oceanography from the Ocean University of China, Qingdao, China, in 2001. He is currently with the Second Institute of Oceanography (SIO), Ministry of Natural Resources (MNR), Hangzhou, where he is also the Head of microwave marine remote sensing, State

Key Laboratory of Satellite Ocean Environment Dynamics (SOED). He has been an Adjunct Professor and a Doctoral Supervisor with Zhejiang University, since 2011, and Hohai University, since 2019. He is also a Senior Member of the Southern Marine Science and Engineering Guangdong Laboratory (Zhuhai). He has more than 20 years' experience in microwave marine remote sensing. He has been a Principal Investigator and a Participant of more than 20 research projects and has published more than 100 scientific articles in peer-reviewed journals and international conference proceedings. His research interests include microwave marine remote sensing, data fusion, image processing, and satellite oceanography.



XIN ZHANG received the Ph.D. degree in physical oceanography from the Scripps Institution of Oceanography, in 1992. He is currently an Emeritus Researcher with the Scripps Institution of Oceanography, University of California at San Diego. After his postdoctoral position at Caltech, he joined the Scripps Institution of Oceanography. His main research interests are in ocean surface dynamics, experimental fluid mechanics, and image processing.

...